Article

Residual Stress and Microstructure of a Ti-6Al-4V Wire Arc Additive Manufacturing Hybrid Demonstrator

Tatiana Mishurova [1,*], **Benjamin Sydow** [2], **Tobias Thiede** [1], **Irina Sizova** [2], **Alexander Ulbricht** [1], **Markus Bambach** [2,3] **and Giovanni Bruno** [1,4]

[1] Bundesanstalt für Materialforschung und–prüfung (Institute for Materials Research and Testing (BAM), 12205 Berlin, Germany; tobias.thiede@bam.de (T.T.); Alexander.Ulbricht@bam.de (A.U.); giovanni.bruno@bam.de (G.B.)

[2] Chair of Mechanical Design and Manufacturing, Brandenburg University of Technology Cottbus-Senftenberg, D-03046 Cottbus, Germany; benjamin.sydow@b-tu.de (B.S.); sizova@b-tu.de (I.S.); bambach@b-tu.de (M.B.)

[3] Advanced Manufacturing, Department of Mechanical and Process Engineering, ETH Zurich, 8092 Zurich, Switzerland

[4] Institute of Physics and Astronomy, University of Potsdam, 14476 Potsdam, Germany

[*] Correspondence: tatiana.mishurova@bam.de; Tel.: +49-30-810-445-27

check for updates

Abstract: Wire Arc Additive Manufacturing (WAAM) features high deposition rates and, thus, allows production of large components that are relevant for aerospace applications. However, a lot of aerospace parts are currently produced by forging or machining alone to ensure fast production and to obtain good mechanical properties; the use of these conventional process routes causes high tooling and material costs. A hybrid approach (a combination of forging and WAAM) allows making production more efficient. In this fashion, further structural or functional features can be built in any direction without using additional tools for every part. By using a combination of forging basic geometries with one tool set and adding the functional features by means of WAAM, the tool costs and material waste can be reduced compared to either completely forged or machined parts. One of the factors influencing the structural integrity of additively manufactured parts are (high) residual stresses, generated during the build process. In this study, the triaxial residual stress profiles in a hybrid WAAM part are reported, as determined by neutron diffraction. The analysis is complemented by microstructural investigations, showing a gradient of microstructure (shape and size of grains) along the part height. The highest residual stresses were found in the transition zone (between WAAM and forged part). The total stress range showed to be lower than expected for WAAM components. This could be explained by the thermal history of the component.

Keywords: residual stress; WAAM; Ti-6Al-4V; additive manufacturing; neutron diffraction; hybrid manufacturing

1. Introduction

The titanium alloy Ti-6Al-4V is intensively used in lightweight applications for the aviation and space industry because of its high specific strength [1]. Hot forging is the usual manufacturing route; this allows better material formation and control of the microstructure. Subsequent machining is used to attain the desired tolerances regarding dimensions, shape, and surface condition [2]. One positive effect of hot forging is that the microstructure and the fiber flow can be optimized, which results in excellent mechanical properties. However, forging is limited as far as the achievable geometries is

concerned: as an example, due to friction and heat transfer, the material cannot flow into cavities of the forging die with a large depth-to-diameter ratio. Moreover, multistage hot forging operations require expensive heated die sets and lead to parts with large tolerances; this requires further machining to create the final shape. In fact, the "buy-to-fly" ratio (the mass ratio between the originally purchased stock material used to produce a part and the mass of the final finished part) ranges from 12:1 to 25:1 for aircraft titanium components made by traditional manufacturing techniques [3]. This means that 12–25 kg of raw material are required to produce just 1 kg of parts. In this way, more than 90% of the material is machined away. Such a high buy-to-fly ratio is unacceptable from many points of view. For a typical titanium component produced by additive manufacturing (AM) techniques the buy-to-fly ratio drops to 3–12:1 [4] and can even be close to 1:1 [5]. By using AM for production of aerospace components not only costs for expensive titanium alloys can be reduced, but also the machining time can be drastically cut.

AM is an innovative manufacturing technology that allows manufacturing almost arbitrarily complex shapes. In powder-bed metal AM processes, the powder is distributed layer-wise on a substrate or already deposited material and fused by melting the material using an electron (electron beam melting–EB-PBF) or laser beam (laser powder bed fusion–L-PBF). Because of the small (focused) beam, the deposition rates are quite low. PBF AM processes have in general a small layer thickness of a few tens of μm up to 2 mm [6]. This is necessary due to the local bonding of adjacent powder particles and the limited beam penetration depth. Although beam scanning systems can achieve high laser or electron beam scanning speeds, large parts require a high number of layers, which causes high production times. The part size is limited due to the small process chamber (typically 200–300 mm edge size). Also, as the powder-bed has to be established before the AM process begins, no existing parts can be extended by means of PBF. This makes this technology only attractive for small parts. An increasingly popular AM technology that may allow overcoming this issue is Wire Arc Additive Manufacturing (WAAM). WAAM utilizes common and well-known welding technologies. A wire is fed to the desired position and molten by an electric arc. The melt pool solidifies and forms a weld bead. One advantage of WAAM compared to other AM technologies is the high deposition rate. This is especially important for large scale products such as landing gear parts or wing ribs, which are difficult to forge due to their size or have a large material waste when machined. WAAM achieves deposition rates as high as several kg/h [7] Also, a wide range of materials is available as wires, which offers multiple possible applications. The microstructure and mechanical performance of WAAM manufactured Ti-6Al-4V parts will not reach the level of forged material without additional (often expensive) post-processing techniques such as hot isostatic pressing (HIP) or thermomechanical processing [8]. One strategy is to combine the benefits of the two technologies (forging and WAAM) to produce so-called hybrid parts with the desired mechanical properties (even at local scale). This approach is of particular interest for the production of the components, where the forged sections are heavily loaded during service and the added AM features should be capable to withstand only moderate loads. Moreover, in aerospace industry many parts possess a symmetry axis. To produce such components by means of conventional processing a number of different forging die sets should be used. Instead, the hybrid approach can be more efficient, since the required structural or functional features can be added to the forged part without using additional tools for every part design. In so doing, both the cost of forging tools and material waste can be reduced. Figure 1 represents a possible hybrid manufacturing route, where the basic structure can be produced by hot forming and the missed structural features can be added using AM.

Basically, two process routes are possible: (i) AM and subsequent forming or (ii) forming and subsequent AM. The first hybrid processing route was extensively studied by authors of the present work in regard to Ti-6Al-4V [9–11]. It was observed that Ti-6Al-4V pre-forms for forging made either by L-PBF or by WAAM show a good hot workability. Moreover, voids could be closed applying compressive stresses at elevated temperature, so that the final microstructure and mechanical properties

could be improved. Extensive work on the second hybrid processing route can also be found in the literature.
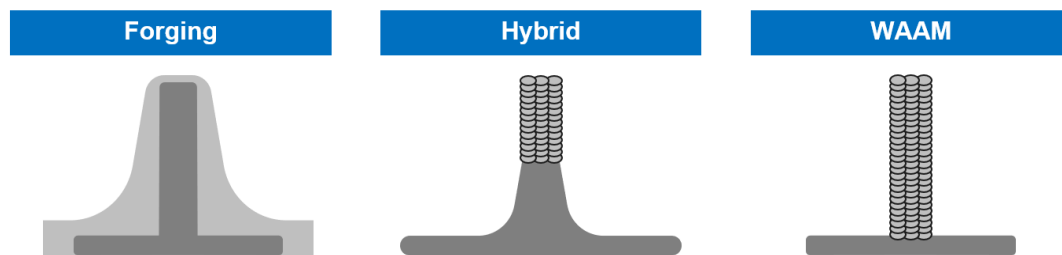
Figure 1. Illustration of the possible hybrid manufacturing route combining metal hot forming and WAAM.

Bambach et al. [11] examined the same demonstrator shape and process route (forging with subsequent WAAM) used in this study and proved that its mechanical properties exceeded the minimum requirements for forged parts regarding yield strength (YS = 837 MPa > 830 MPa) and ultimate tensile strength (UTS = 934 MPa > 900 MPa). Also, only minor anisotropic behavior was observed. In another work, Bambach et al. [12] showed that laser cladding technology could be used to produce flexibly applicable local patches to locally increase the stiffness or the thickness of sheet metal components. Papke et al. [13] analyzed tensile bonding strength of hybrid parts made of Ti-6Al-4V produced by combination of laser beam melting and warm bending. It was reported, that sheet material and AM material possess different hardness values, and the sheet thickness strongly influences the bonding strength. Moreover, it was confirmed, that the contact zone between sheet and AM is the most significant for the strength of hybrid components [14]. Hirtler et al. [15] investigated the production of modifying stiffening ribs made of AlSi12 on conventionally produced pre-forms (EN-AW 6082). The authors proved the feasibility of the process combination between WAAM and hot forming. In general, most of the existing work on hybrid manufactured of Ti-6Al-4V concentrates on the increase of the strength of the sheet metal components using AM.

To produce a sound Ti-6Al-4V hybrid part the microstructure should be thoroughly controlled. During WAAM of Ti-6Al-4V β-grains (BCC) grow epitaxially, similar to PBF AM techniques [16]. Such microstructures are hard to avoid because at the low concentration Al and V have a high solubility in the alloy and, thus, do not partition ahead of the solidification front [17]. The length of prior β grains along the solidification direction can reach a few cm or even cover the whole height of the sample, possessing a strong <001> fiber texture [18]. After cooling below the β-transus temperature (approximately 995 ± 25 °C) β grains typically transform to fine α laths (HCP) retaining β lamellar structure (Widmanstätten structure). Here the thickness of α-platelets and the sizes of β-grains are the fundamental parameters that affect the mechanical performance of Ti-6Al-4V alloy. Very high cooling rates (>410 °C/s) promote martensitic transformation. Slower cooling rates (<20 °C/s) promote formation of Widmanstätten microstructures [19]. Furthermore, the cooling rate determines the thickness and the presence of α-phase on prior β grain boundaries, which strongly affect the mechanical performance, because they induce anisotropy [20]; such anisotropy is unwanted in many applications. In general, the Widmanstätten-type microstructure is characterized by relatively low tensile ductility, good creep resistance, moderate fatigue properties and crack growth resistance [21].

Together with the microstructure, residual stress (RS) is one of the major obstacles in the development of the AM techniques [22]. It may lead to cracking and geometrical distortion of the parts, thereby limiting the design freedom of the component [23,24]. In the case of WAAM, RS is also an important factor influencing the structural integrity [20]. Colegrove et al. have reported that in as-deposited state the RS values in steel WAAM part can reach the yield stress of the material [25]. Also, the presence of RS highly affects the mechanical behavior of the part. Zhang et al. have reported [26] that RS facilitates crack propagation from a WAAM Ti-6Al-4V part to its substrate. One of the strategies for the reduction of RS and the refinement of the microstructure in WAAM is high pressure rolling after

every deposited layer (or a few of them) [25,27]. This approach, however, imposes some limitations on the part design and degrades the main advantage of the WAAM technique: the high deposition rates. In general, according to ASTM F2924 [28], stress-relief heat treatment is mandatory for Ti-6Al-4V AM parts. The connection between microstructure and RS for welded and AM materials has been reported in several studies [29–32]. Due to high cooling rate needed for martensitic transformation ($\beta \rightarrow \alpha'$) in Ti-6Al-4V, the martensitic microstructure is often linked with high tensile RS [30]. It has been shown that the presence of β phase in PBF Ti-6Al-4V, introduced by intrinsic heat treatment, leads to the RS relaxation [31]. Thus, for the general application of WAAM, it is important to understand the microstructure and the RS in as-manufactured WAAM components. Such properties depend also on the location in the hybrid part. An investigation of the microstructure and the RS at the interface between forged and AM features is here of particular importance. In AM parts, high tensile RS is usually reached at the interface between the substrate and the deposited material [33]. This could be critical for the utilization of hybrid parts.

The main aim of the current study is to investigate the microstructure and the RS distribution in a hybrid part produced by the combination of conventional hot forming and WAAM. A T-section geometry manufactured by means of WAAM on a hot forging pre-form is investigated. The paper is structured as follows: Section 2 presents the manufacturing of hybrid Ti-6Al-4V parts using WAAM and hot forging. Also, the procedures of microstructural analysis and of determination of RS by means of neutron diffraction are presented. Section 3 gives an overview of results of metallographic examinations and RS. Finally, the results are discussed, and conclusions are presented.

2. Materials and Methods

2.1. Sample Manufacturing

The considered hybrid process route encompassed forging and subsequent WAAM of Ti-6Al-4V. A T-shaped pre-form was forged, as shown in Figure 2. It contained a 10 mm wide and ~90 mm long rib, which was milled flat at a total height of 42 mm. The WAAM process was used to increase the height of the rib by 66 mm.

Hot forging was performed in the $\alpha + \beta$-temperature range using a 2500 t crank press at OTTO FUCHS KG (Meinerzhagen, Germany). The forged part was machined on the top side to obtain a flat surface to ensure a stable WAAM process.
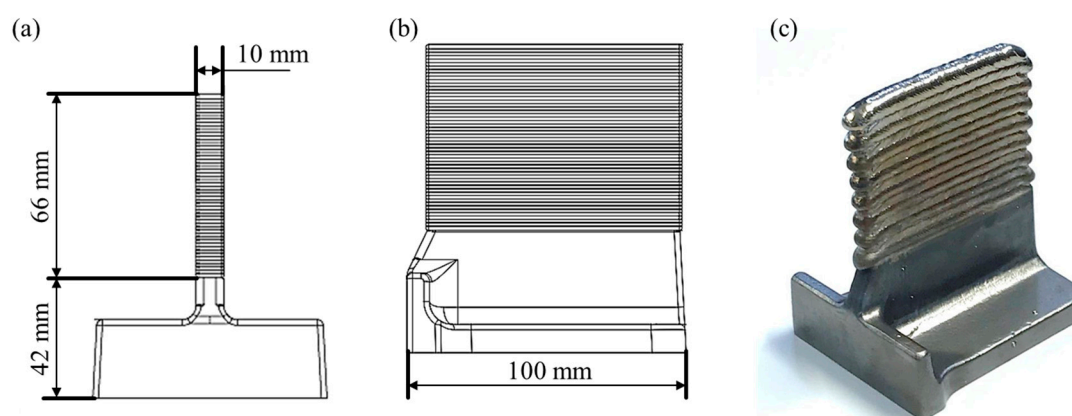
Figure 2. Drawing of the final pre-form with dimensions. Front view (**a**), side view (**b**), final appearance of the hybrid near-net shape demonstrator (**c**).

WAAM was performed using a Fanuc six-axis robot (FANUC Europe Corporation S. A., Echternach, Luxembourg) and a TPS 500i welding power source (Fronius®, Wels, Austria) utilizing the Cold Metal Transfer (CMT) variant of the Gas Metal Arc Welding (GMAW) process. The welding was carried out in an argon filled, sealed chamber to avoid oxidation. The chamber was equipped with an O_2

sensor. Pre-heating of the sample was not applied. The used WAAM set-up is displayed in Figure 3a. A Ti-6Al-4V wire with a diameter of 1.0 mm was used. One hybrid demonstrator was produced for investigations. The shielding gas flow rate at the torch was 15 L/min, also the build chamber was flooded with 50 L/min before the deposition process. During deposition the chamber gas flow rate was reduced to 20 L/min to compensate the small gas leakage. The argon gas purity was ≥99.99%. The chemical composition for as-built Ti-6Al-4V WAAM is shown in Table 1.
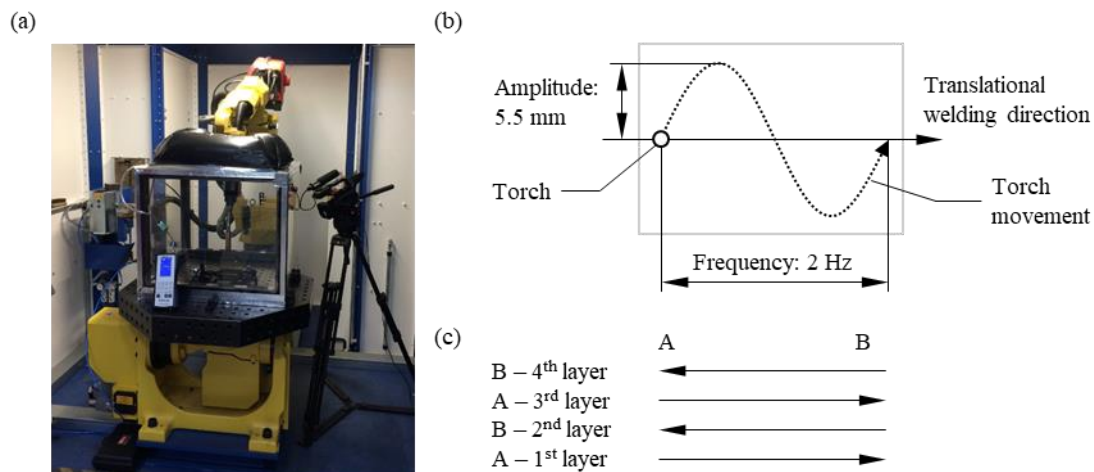
Figure 3. For the WAAM process (**a**) used WAAM machine, (**b**) applied sinus wave movement and (**c**) swapping of the starting point each layer.

Table 1. Chemical composition of Ti-6Al-4V as-built by WAAM (max. weight %).

Ti	Al	V	Fe	C	Other
Bal.	6.45	3.87	0.19	0.07	0.17

The deposition pattern is shown in Figure 3b,c. The starting point (A/B) changed for every layer using a bidirectional tool path on a single bead. A sinus wave was superposed onto the translational motion of the torch to obtain the desired wall thickness. The layer thickness was approximately 4.4 mm. The number of deposited layers was 15.

The welding parameters are shown in Table 2. The first three layers were welded with a higher electrical current to achieve a good fusion with the forged substrate and to increase the average temperature (this ensures a stable WAAM process). The current was than reduced to 100 A for the following layers.

Table 2. WAAM manufacturing parameters.

| Parameter	Value
Wire diameter	1.0 mm
Amplitude	5.5 mm
Frequency	2 Hz
Welding speed	15 cm/min
Cooling time between deposition of each layer	130 s
Average electrical voltage	13.5 V
Average electrical current	1st layer: 135 A 2nd layer: 115 A 3rd layer: 105 A ≥4th layers: 100 A

2.2. Microstructural Characterization

In order to investigate the microstructure, the manufactured hybrid part (including the forged region) was cut along the build direction. The sample was mounted with the cut cross-sections on top and ground flat with successively finer grades (from 320 to 1200 μm) of silicon carbide (SiC) papers. The specimen was then polished with 0.05 μm silica solution (OP-S Suspension, Struers GmbH, Willich, Germany) with the addition of H_2O_2, HNO_3, and HF. Sample was etched with Kroll's agent solution to reveal the microstructure. The sections were analyzed using an optical microscope Carl Zeiss Axiotech by Carl Zeiss Microscopy (Jena, Germany).

2.3. Residual Stress Analysis

The neutron diffraction experiment was conducted on the instrument E3 at BER II reactor (Helmholtz Zentrum Berlin, Germany) [34]. A monochromatic neutron beam of wavelength λ = 1.476 Å was used. The three orthogonal strain components, assumed to be principal directions based on the sample geometry, were measured (longitudinal, transversal, normal, see Figure 4). The longitudinal and normal directions coincided with the deposition and the build direction of WAAM, respectively. The acquisition time was set to 75 min for each stress component. Additionally, to improve the diffraction signal, a constant ω oscillation of ±10° around the scattering vector (this is the bisectrix between the incident and the diffracted beam directions and corresponds to the direction in which the strain is measured) was performed. For the longitudinal stress component, a primary slit with opening of 4 mm × 4 mm was used. For the normal and transversal component, a primary slit with vertical opening of 18 mm and horizontal opening of 2 mm was used. This allowed at the same time increasing the signal and keeping high spatial resolution along the build direction of the sample. A secondary collimator with a focus of 2 mm was used for all measurements. The strain was measured along two lines: along the deposition direction at the middle height of the WAAM part (L-line) and along the build direction (N-line). The measured points and coordinate system are schematically presented in Figure 4a.
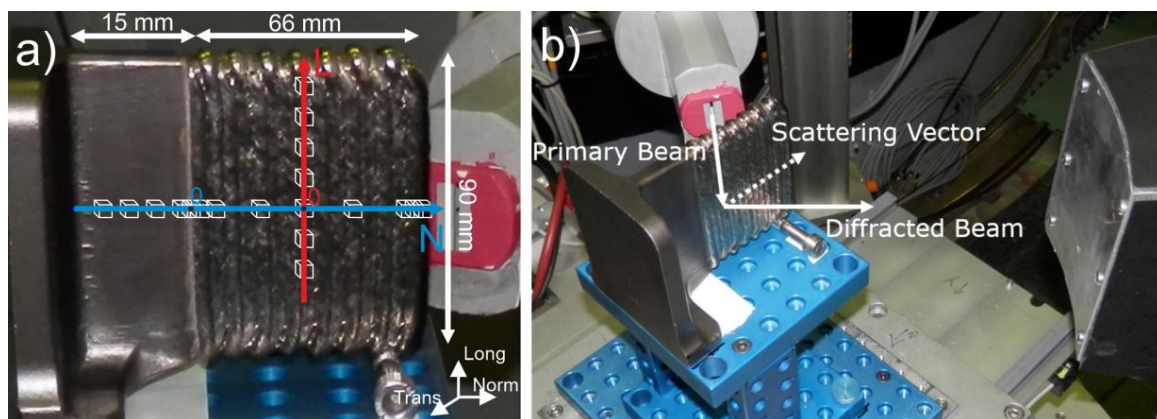
Figure 4. Photo of sample during neutron diffraction experiment on E3 with the schematics of (**a**) the measured points and the coordinate system, (**b**) the set-up. (Note that the sample is aligned for the measurement on the normal strain component).

The measurements were performed at the diffraction angle 2θ = 76°, which allowed the simultaneous detections of three diffraction peaks for α-Ti: $11\bar{2}2$, $20\bar{2}1$ and 0004. However, only the $11\bar{2}2$-α reflection appeared at every measured point and sample direction, therefore the RS was calculated for this crystallographic family. The lattice spacing *d* was calculated according to Bragg's law:

$$d_{11\bar{2}2} = \frac{\lambda}{2 \cdot \sin\theta_{11\bar{2}2}} \tag{1}$$

The lattice spacing (averaged within the gauge volume) was determined by fitting the diffraction peak with a Gaussian function using the software StressTexCalculator 1.53 (TU-Clausthal, Germany). In order to calculate lattice strains ε a strain-free reference d_0 has to be used, since:

$$\varepsilon = \frac{d_{11\bar{2}2} - d_0}{d_0} = \frac{\sin\theta_0}{\sin\theta_{11\bar{2}2}} - 1 \tag{2}$$

One of the main problems in diffraction-based RS analysis is the estimation of such a reference [35,36]. There are different approaches for the determination of d_0: measurements using a reference powder or stress-relieved coupons; or calculations using a global average or stress balance/boundary conditions. In the case of AM materials the variation of the microstructure inside the part and the different thermal history of the part from the raw material (power, wire) makes the determination of d_0 even more challenging [35]. In our case, a global d_0 (or θ_0) was taken as the average of all measured points, as proposed in [37]. This value was $2\theta_0 = 72.856°$ with an average error of $\pm0.007°$ (coming from the fit of all diffraction peaks). As an alternative, the stress balance condition was applied to the L-line scan for the normal component (Figure 4): $\int \sigma_{Norm} dL = 0$. For this estimation the stress profile was extrapolated to the surface and interpolated between the points with a B-spline function. Symmetry of the stress profile was assumed, i.e., $\sigma_N(+L) = \sigma_N(-L)$. Using this approach, we obtained $2\theta_0 = 72.859°$. This value lies within the error range of the $2\theta_0$ obtained using the global average approach and shifts the resulting stress values only by +10 MPa. Therefore, only stress profiles calculated satisfying the above-mentioned stress balance conditions will be reported.

RS were calculated according to the tensorial Hooke's Law: $\sigma = C\varepsilon$, with $\boldsymbol{C}$ as the stiffness tensor. With the assumption that the principal geometric directions are also principal stress directions, Hooke's Law in the case of a quasi-isotropic solid reads:

$$\sigma_{L,T,N} = \frac{E^{11\bar{2}2}}{\left(1 + \nu^{11\bar{2}2}\right)\left(1 - 2\nu^{11\bar{2}2}\right)}\left[\left(1 - \nu^{11\bar{2}2}\right)\varepsilon_{L,T,N} + \nu^{11\bar{2}2}\left(\varepsilon_{T,N,L} + \varepsilon_{N,L,T}\right)\right] \tag{3}$$

where $\sigma_{L,T,N}$ and $\varepsilon_{L,T,N}$ are stresses and strains along the longitudinal, transversal and normal direction, and $E^{11\bar{2}2} = 112.7$ GPa and $\nu^{11\bar{2}2} = 0.321$ are the diffraction elastic constants for α-Ti $11\bar{2}2$ reflection calculated by the Kröner's model [38].

Hydrostatic stress σ_H and von Mises stresses σ_{vM} were calculated according to:

$$\sigma_H = \frac{\sigma_T + \sigma_L + \sigma_N}{3} \tag{4}$$

$$\sigma_{vM} = \sqrt{\frac{1}{2}\left[(\sigma_L - \sigma_T)^2 + (\sigma_T - \sigma_N)^2 + (\sigma_N - \sigma_L)^2\right]} \tag{5}$$

3. Results and Discussion

Figures 5 and 6 show the macro- and microstructure of the hybrid part, respectively. To interpret the microstructural features, we must recall that the first layers were produced with higher current (see Table 2) to compensate the heat sink effect of the substrate. Then, the heat input (i.e., current) was gradually decreased, and after the fourth layer it was set to a constant value. The macrostructure of the WAAM Ti-6Al-4V is characterized by the epitaxial growth of large columnar prior β-grains, which stretch through several deposited layers (Figure 5). The average dimensions of such grains are about 1.3 mm perpendicular and 8 mm parallel to the build direction.
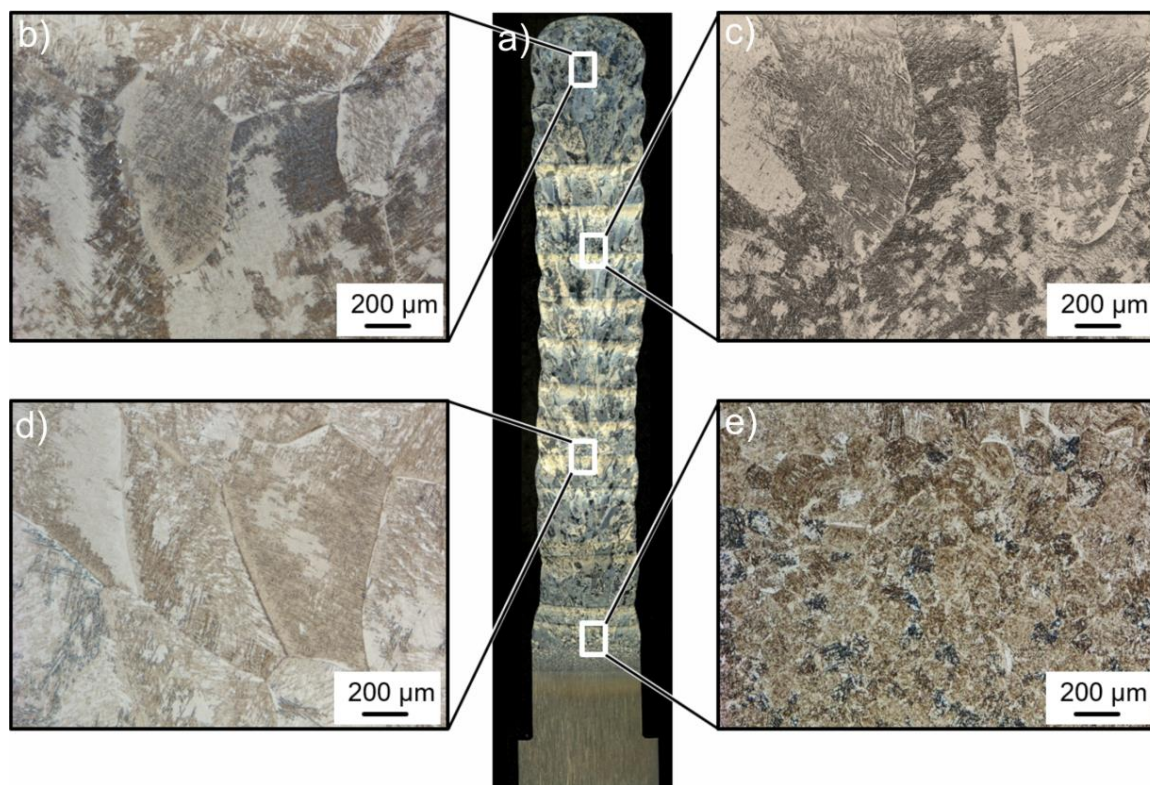
Figure 5. (**a**) Micrograph showing prior β-Ti grains in the middle section of the sample with enlarged view for (**b**) top of WAAM part, (**c,d**) middle height of WAAM part, (**e**) transition region between WAAM and forged parts.
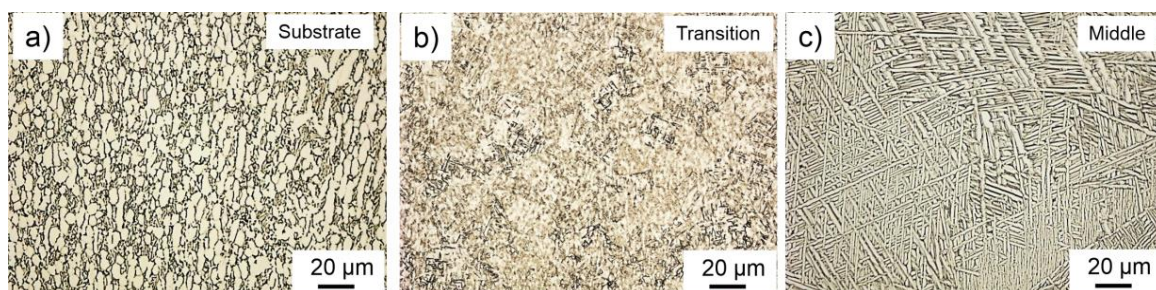

Figure 6. Typical micrographs obtained (**a**) in the substrate, (**b**) in the transition zone close to the substrate, (**c**) in the center of the WAAM part.

The forged Ti-6Al-4V T-section shows, instead, a bi-modal α+β microstructure (Figure 6a), typically obtained in Ti-6Al-4V after conventional thermomechanical processing [21]. The first layers of the WAAM material are characterized by a higher cooling rate compared to the following layers, due to heat conduction to the substrate. Therefore, in the transition zone (e.g., in the first layers, up to approximately 7 mm distance from the seam line), a fine martensitic α' microstructure is found within small globular prior β-grains with average dimensions of approximately 50 μm (Figure 6b).

At sample mid-height, the micrographs show an $α_w$-Widmanstätten microstructure with a thickness of the α-platelets of approximately 2 μm within the columnar prior β-grains (Figure 6c). Such microstructures are often reported in the literature [3]. Moreover, the α-phase also appears as a thin layer on the prior β-grain boundaries with a thickness comparable to the thickness of the α-platelets. This microstructure was generated by the repeated rapid heating and cooling that occur during the WAAM process. It is important to stress that the coarse prior β grains may critically affect the mechanical properties (since β is more ductile than α).

A flat panel detector was used in the neutron diffraction experiment. The 2D distributions of the diffraction signal give valuable information about the microstructure (Figure 7): especially in the longitudinal direction, diffraction spots (instead of the typical Debye rings observed for polycrystalline materials) were observed. This is called the "coarse grain effect" (Figure 7a). The grain size of α-Ti laths is quite small, with an average thickness of about 2 μm and an average length of about 25 μm (see Figure 6). However, the origin of α-Ti laths create a distinct crystallographic texture. All the grains of α-Ti inside the prior β-grain are only variants of the same crystallographic orientation, according to Burgers orientation relation [39]. Thus, from the crystallographic point of view, such laths form coarse grains, which scatter similarly to single crystals in the longitudinal direction. In spite of this effect, the projections of the few spots inside a 2D detector image could be analyzed as a Bragg peak, and the lattice parameter could be reliably determined.
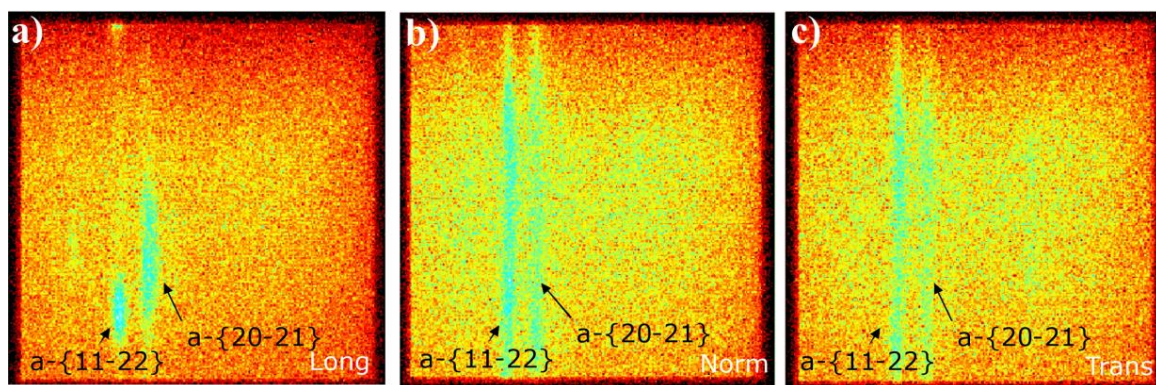
Figure 7. Image of 2D detector obtained during neutron diffraction experiment on the WAAM part (at 46 mm) for (**a**) longitudinal direction, (**b**) normal direction, (**c**) transversal direction. Note: the images are normalized to the maximum intensity, the pixel size is 1.17 mm × 1.17 mm.

The neutron diffraction patterns (i.e., integrated along the Debye ring) collected along the L-line for three orthogonal directions are presented in Figure 8. The patterns look similar at every position, thereby showing no microstructural variations along the deposition direction. The peak intensities (of both $11\bar{2}2$ and $20\bar{2}1$ reflections) do not vary for different orientations, highlighting the absence of a strong crystallographic texture.
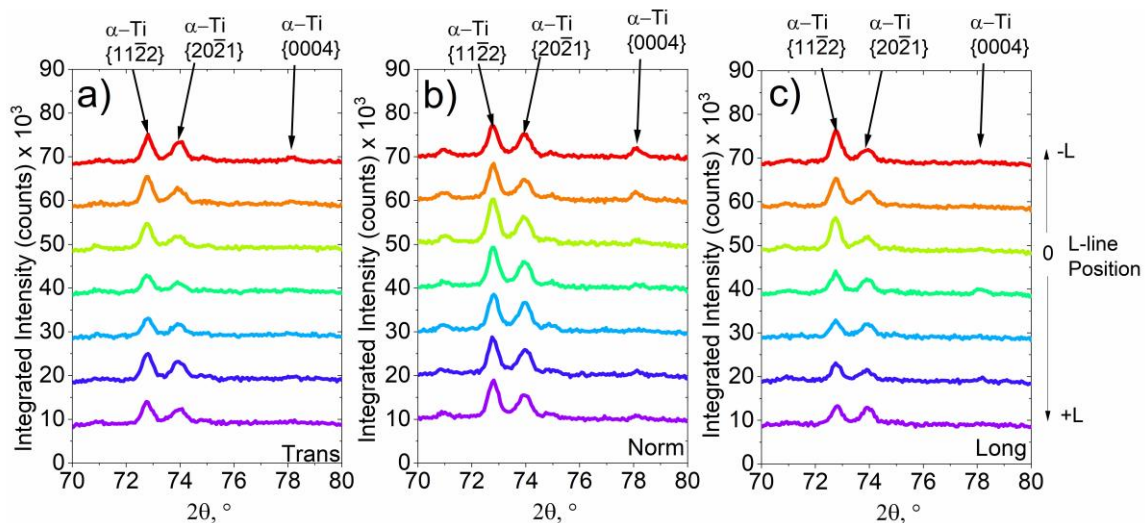
Figure 8. Diffraction patterns along the L-line for (**a**) transversal component, (**b**) normal component, (**c**) longitudinal component.

The intensity ratios follow the theoretical predictions for the neutron diffraction pattern of HCP-Ti powder (i.e., assuming random crystallographic texture, calculated by PowderCell [40]): the intensity of the $11\bar{2}2$ reflection is the highest out of the three reflections observed, followed by $20\bar{2}1$ and 0004 reflection.

In contrast to the diffraction patterns acquired along the deposition direction (L-line, Figure 8), a decrease of the intensity towards the substrate for all reflections of the transversal strain component can be observed along the build direction (Figure 9a). As shown in Figure 2, the thickness of the sample is the same as the thickness of the substrate (in the analyzed region up to 15 mm of substrate), so this cannot be caused by higher neutron absorption. In other words, the path of the neutron beam stays the same for the WAAM and the forged part. Therefore, this intensity variation is an evidence of the microstructural changes reported in Figure 6 and, in particular, of the crystallographic texture. The ratio between the $11\bar{2}2$ and $20\bar{2}1$ peak intensities changes with the height for the longitudinal component (Figure 9c). The 0004 peak increases its intensity for the points in the transition zone and inside the substrate for the normal component (Figure 9b). Thus, an increase in intensity from the prismatic crystallographic plane (1000) for the transversal component could be expected. Since we mostly observed mixed reflections ($11\bar{2}2$ and $20\bar{2}1$), it is hard (and anyway out of the scope of this study) to quantify the effect of crystallographic texture from the current experiments.
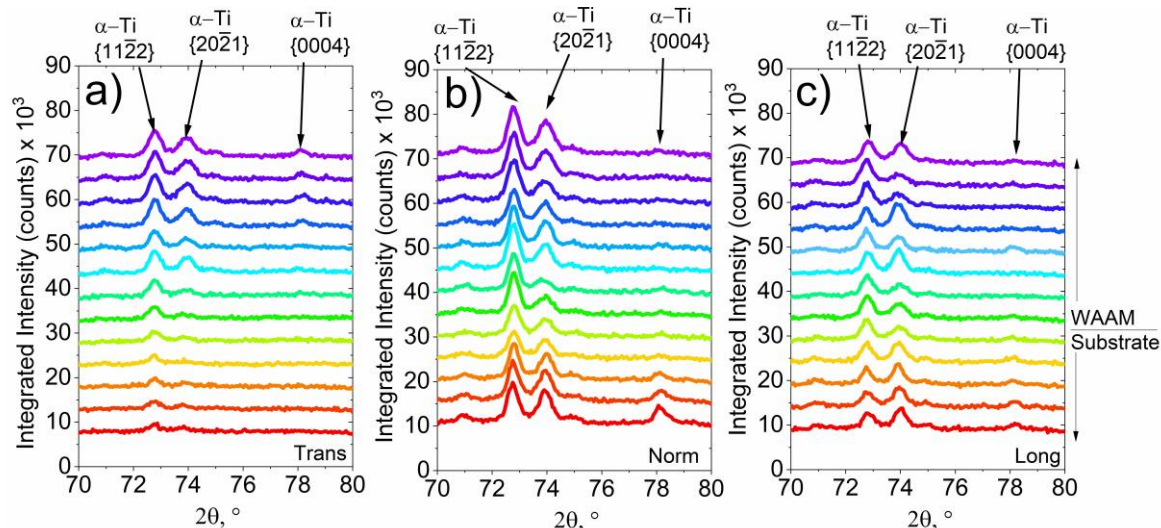

Figure 9. Diffractograms along the N-line for (**a**) transversal component, (**b**) normal component, (**c**) longitudinal component.

The normalized integrated intensity and the full width at half maximum (FWHM) of diffraction peaks along the N-line are presented in Figure 10. Although the coarse grain effect was observed for the longitudinal component (Figure 7a), the FWHM and the integrated intensity of the peak did not vary within the sample (Figure 10b). As for the transition zone and for the substrate, the intensity drops for each measured strain component. In the substrate (Figure 6a), the intensity increases for the normal component. This can be caused by microstructural and crystallographic texture changes (see Figures 5 and 6). It should be noticed that most changes happen in the transition region (from +10 mm to −10 mm) and stabilize inside the WAAM section and the substrate. An increase of the FWHM is often connected to plastic deformation of the material, however, in the present case the FWHM remains constant for the whole height of the sample. Only the transversal component of some points in the substrate shows an increase of the FWHM; this is an artifact due to the low intensity of the peaks (i.e., higher fitting error), see Figure 9a.
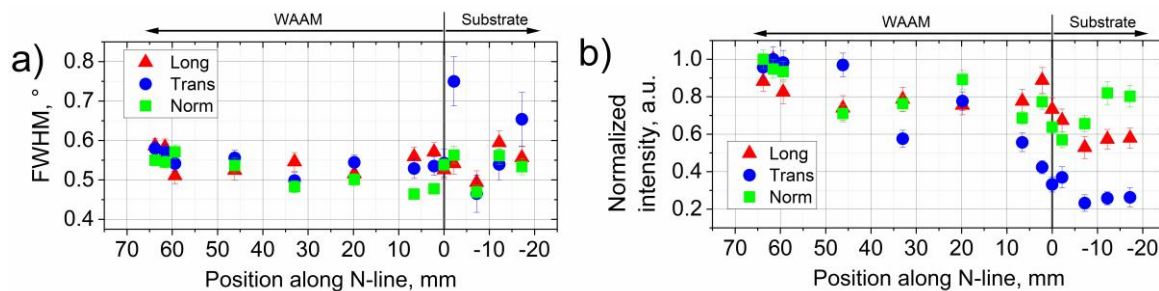
Figure 10. (**a**) FWHM and (**b**) normalized integrated intensity of the $11\bar{2}2$ -Ti diffraction peak along the build direction.

The hydrostatic σ_H and von Mises stress σ_{vM} profiles along L- and N-lines are presented in Figure 11. The stress range for both is around 100 MPa. The hydrostatic stresses cannot be released by post-processing heat treatment and, hence, could be critical for structural integrity of the part under load. In the present case, σ_H reaches its maximum value of around 75 MPa, this is only 10% of the yield stress of WAAM Ti-6Al-4V (around 750 MPa according to [41]). While this value is not critical for the part integrity, it should be taken into account when assessing the life of the component (e.g., under fatigue).
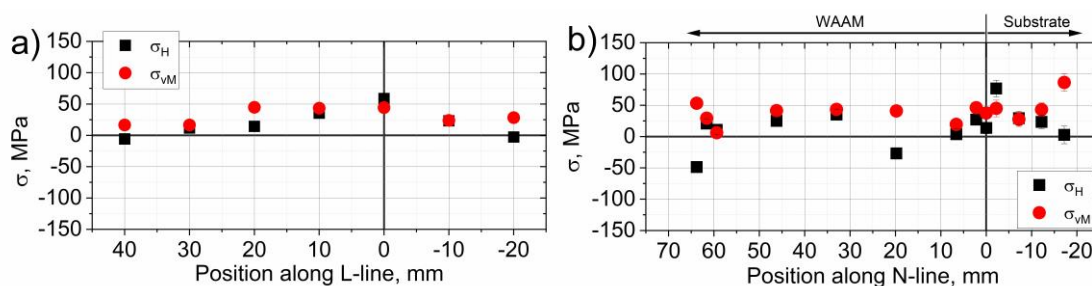

Figure 11. Hydrostatic and von Mises stress along (**a**) L-line, (**b**) N-line. Error bars are contained in the markers.

The longitudinal RS profile along the sample L-line shows a maximum (about 100 MPa) in the middle of the sample (Figure 12a). The profile is symmetric and is similar to that simulated by Ding et al. [42] for steel WAAM parts. The stress profiles along N-line are more complicated (Figure 12b). In the literature the longitudinal component of the RS (coinciding with the deposition direction) usually shows the highest values and the highest gradients. Several experimental RS determination methods (such as the contour method [43] and neutron diffraction [44]) and modeling [42] have revealed the typical longitudinal RS profile generated along the height of WAAM parts. There is some consensus that high tensile stress appears in the region near the substrate and constantly decreases to compressive towards the top of the sample (see schematic in Figure 12c). This is also typical for stress profiles across heterogeneous junctions (see e.g., [45]). The RS rapidly decreases from the transition zone (WAAM/substrate) to the bottom of the substrate. In fact, the whole part should satisfy the stress balance conditions. In our case, the RS decreases to around −50 MPa at 20 mm and then increases to slightly tensile values and decreases again at the very top of the sample (Figure 12b). This follows typical RS profiles (see Figure 12c), with the exception of the point at 20 mm. As mentioned above, during production the energy input was decreased for the first four layers (around 18 mm, see Table 2); therefore, this region of the sample had different thermal input compared to the rest of the WAAM part. This may also be the reason why in this region low RS is found. The sensitivity of RS to variations of the production parameters has been reported for many AM materials [31,36].

Along the build direction all components of the RS lie in the range between −100 MPa and 100 MPa (Figure 12b). This stress range is lower than that reported for WAAM Ti-6Al-4V (reaching around 600–700 MPa [33,37,43,44], with a maximum tensile stress value of around 500 MPa). High RS could be

induced by large cooling rates, which are favored by large contact areas (WAAM fabrication, Figure 1) and small substrate thickness, as they were used in the cited works. In the present study, the part of the pre-form used as substrate (a thin upright wall, as in hybrid fabrication, Figure 1), allowed a larger heat accumulation. In this case the geometry of the hybrid part played an important role in RS formation. Furthermore, the used deposition strategy with a sinusoidal path induced a higher energy per unit length (Figure 3b). Thus, the average temperature level was higher during production. This caused a lower temperature gradient, lower flow stresses, and, therefore, smaller RS. Furthermore, the repeated sinusoidal passes induced a so-called intrinsic heat treatment (IHT), analogous to certain scan strategies for L-PBF (see e.g., [31,36]), thereby offering a mechanism for RS relaxation.
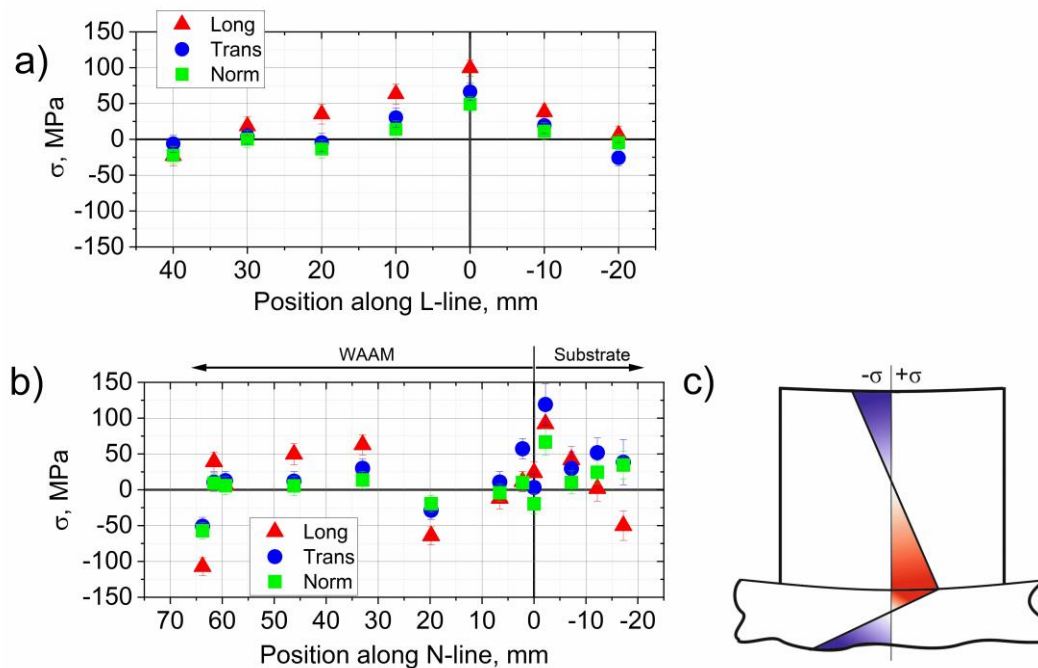
Figure 12. RS profile (**a**) along the L-line and (**b**) along the N-line, (**c**) schematic of the typical stress profile along the WAAM sample height.

4. Summary

We investigated a so-called hybrid Ti-6Al-4V part, made of a WAAM wall and a forged T-shape substrate. Such a component showed the following microstructure along its height: bi-modal ($\alpha+\beta$) in the forged part, martensitic in the transition zone, and Widmanstätten laths inside the WAAM part (as observed by optical microscopy). Neutron diffraction patterns revealed the presence of preferential crystallographic orientation, changing along the sample height (build direction) but not within deposited layers. Residual stress analysis in the bulk of such hybrid part (by means of neutron diffraction) showed a strong stress gradient in the transition region for every stress component. The hybrid forging+WAAM production induced lower residual stress (maximum values around 100 MPa) compared to purely WAAM components reported in the literature (with maximum stress around 500 MPa). We explained such a low stress by the higher heat accumulation and lower cooling rate during hybrid production (the thin substrate hinders heat accumulation), as well as by the sinusoidal shape of the torch movement. An intrinsic heat treatment (successive sinusoidal passes) also assists stress relaxation. The residual stress profiles along the build direction are also expected to be affected by the heat input variation within the part during production. Simulation work is ongoing to understand the formation of residual stress and microstructure in such hybrid WAAM parts.

References

1. Boyer, R.R. An overview on the use of titanium in the aerospace industry. *Mater. Sci. Eng. A* **1996**, *213*, 103–114. [CrossRef]

2. Beal, J.D.; Boyer, R.; Sanders, D. Forming of Titanium and Titanium Alloys. In *Metalworking: Sheet Forming*; Semiatin, S.L., Ed.; ASM International: Geauga, OH, USA, 2006; Volume 14B.

3. Huang, R.; Riddle, M.; Graziano, D.; Warren, J.; Das, S.; Nimbalkar, S.; Cresko, J.; Masanet, E. Energy and emissions saving potential of additive manufacturing: The case of lightweight aircraft components. *J. Clean. Prod.* **2016**, *135*, 1559–1570. [CrossRef]

4. Allen, J. An Investigation into the Comparative Costs of Additive Manufacture vs. Machine from Solid for Aero Engine Parts. In *Cost Effective Manufacture via Net-Shape Processing, Proceedings of the Meeting Proceedings RTO-MP-AVT-139, 15–17 May 2006, Amsterdam, The Netherlands*; RTO: Neuilly-sur-Seine, France, 2006; p. 171-1.

5. Dutta, B.; Froes, F.H. Chapter 1—The Additive Manufacturing of Titanium Alloys. In *Additive Manufacturing of Titanium Alloys*; Dutta, B., Froes, F.H., Eds.; Butterworth-Heinemann: Oxford, UK, 2016; pp. 1–10. [CrossRef]

6. DebRoy, T.; Wei, H.L.; Zuback, J.S.; Mukherjee, T.; Elmer, J.W.; Milewski, J.O.; Beese, A.M.; Wilson-Heid, A.; De, A.; Zhang, W. Additive manufacturing of metallic components—Process, structure and properties. *Prog. Mater. Sci.* **2018**, *92*, 112–224. [CrossRef]

7. Williams, S.W.; Martina, F.; Addison, A.C.; Ding, J.; Pardal, G.; Colegrove, P. Wire + Arc Additive Manufacturing. *Mater. Sci. Technol.* **2016**, *32*, 641–647. [CrossRef]

8. Martina, F.; Williams, S.; Colegrove, P. Improved microstructure and increased mechanical properties of additive manufacture produced TI-6AL-4V by interpass cold rolling. In Proceedings of the 24th International Solid Freeform Fabrication Symposium, Austin, TX, USA, 12–14 August 2014.

9. Sizova, I.; Hirtler, M.; Günther, M.; Bambach, M. Wire-arc additive manufacturing of pre-forms for forging of a Ti–6Al–4V turbine blade. In Proceedings of the 22nd International Conference on Material Forming, Vitoria-Gasteiz, Spain, 8–10 May 2019; p. 150017.

10. Bambach, M.; Sizova, I.; Emdadi, A. Development of a processing route for Ti-6Al-4V forgings based on preforms made by selective laser melting. *J. Manuf. Process.* **2019**, *37*, 150–158. [CrossRef]

11. Bambach, M.; Sizova, I.; Sydow, B.; Hemes, S.; Meiners, F. Hybrid manufacturing of components from Ti-6Al-4V by metal forming and wire-arc additive manufacturing. *J. Mater. Process. Technol.* **2020**, *282*, 116689. [CrossRef]

12. Bambach, M.; Sviridov, A.; Weisheit, A.; Schleifenbaum, J. Case Studies on Local Reinforcement of Sheet Metal Components by Laser Additive Manufacturing. *Metals* **2017**, *7*, 113. [CrossRef]

13. Papke, T.; Huber, F.; Geyer, G.; Schmidt, M.; Merklein, M. Characterisation of the Tensile Bonding Strength of Ti-6Al-4V Hybrid Parts Made by Sheet Metal Forming and Laser Beam Melting. In *Advances in Production Research*; Schmitt, R.G.S., Ed.; Springer: Cham, Switzerland, 2019.

14. Butzhammer, L.; Dubjella, P.; Hubera, F.; Schaub, A.; Aumüller, M.; Baum, A.; Petrunenko, O.; Merklein, M.; Schmidt, M. Experimental investigation of a process chain combining sheet metal bending and laser beam melting of Ti-6Al-4V. In Proceedings of the World of Photonics Congress: Lasers in Manufacturing, Munich, Germany, 26–29 June 2017.

15. Hirtler, M.; Jedynak, A.; Sydow, B.; Sviridov, A.; Bambach, M. Investigation of microstructure and hardness of a rib geometry produced by metal forming and wire-arc additive manufacturing. In Proceedings of the 5th MATEC Web of Conferences, Bremen, Germany, 18–21 September 2018; EDP Sciences: Les Ulis, France, 2018; p. 02005.

16. Antonysamy, A.A.; Meyer, J.; Prangnell, P.B. Effect of build geometry on the β-grain structure and texture in additive manufacture of Ti6Al4V by selective electron beam melting. *Mater. Charact.* **2013**, *84*, 153–168. [CrossRef]

17. Bermingham, M.J.; McDonald, S.D.; Dargusch, M.S.; StJohn, D.H. Grain-refinement mechanisms in titanium alloys. *J. Mater. Res.* **2011**, *23*, 97–104. [CrossRef]

18. Wang, F.; Williams, S.; Colegrove, P.; Antonysamy, A.A. Microstructure and Mechanical Properties of Wire and Arc Additive Manufactured Ti-6Al-4V. *Metall. Mater. Trans. A* **2012**, *44*, 968–977. [CrossRef]

19. Ahmed, T.; Rack, H.J. Phase transformations during cooling in a+b titanium alloys. *Mater. Sci. Eng. A* **1998**, *243*, 206–211. [CrossRef]

20. Wu, B.; Pan, Z.; Ding, D.; Cuiuri, D.; Li, H.; Xu, J.; Norrish, J. A review of the wire arc additive manufacturing of metals: Properties, defects and quality improvement. *J. Manuf. Process.* **2018**, *35*, 127–139. [CrossRef]

21. Leyens, C.; Peters, M. *Titanium and Titanium Alloys: Fundamentals and Applications*; Wiley-VCH Verlag GmbH & Co. KGaA: Hoboken, NJ, USA, 2003.

22. Liu, S.; Shin, Y.C. Additive manufacturing of Ti6Al4V alloy: A review. *Mater. Des.* **2019**, *164*, 107552. [CrossRef]

23. Yadroitsev, I.; Yadroitsava, I. Evaluation of residual stress in stainless steel 316L and Ti6Al4V samples produced by selective laser melting. *Virtual Phys. Prototyp.* **2015**, *10*, 67–76. [CrossRef]

24. Patterson, A.E.; Messimer, S.L.; Farrington, P.A. Overhanging Features and the SLM/DMLS Residual Stresses Problem: Review and Future Research Need. *Technologies* **2017**, *5*, 15. [CrossRef]

25. Colegrove, P.A.; Coules, H.E.; Fairman, J.; Martina, F.; Kashoob, T.; Mamash, H.; Cozzolino, L.D. Microstructure and residual stress improvement in wire and arc additively manufactured parts through high-pressure rolling. *J. Mater. Process. Technol.* **2013**, *213*, 1782–1791. [CrossRef]

26. Zhang, J.; Wang, X.; Paddea, S.; Zhang, X. Fatigue crack propagation behaviour in wire+arc additive manufactured Ti-6Al-4V: Effects of microstructure and residual stress. *Mater. Des.* **2016**, *90*, 551–561. [CrossRef]

27. Donoghue, J.; Antonysamy, A.A.; Martina, F.; Colegrove, P.A.; Williams, S.W.; Prangnell, P.B. The effectiveness of combining rolling deformation with Wire–Arc Additive Manufacture on β-grain refinement and texture modification in Ti–6Al–4V. *Mater. Charact.* **2016**, *114*, 103–114. [CrossRef]

28. ASTM. *ASTM F2924—Standard Specification for Additive Manufacturing Titanium-6 Aluminum-4 Vanadium with Powder Bed Fusion*; ASTM: West Conshohocken, PA, USA, 2014.

29. Mehdi, B.; Badji, R.; Ji, V.; Allili, B.; Bradai, D.; Deschaux-Beaume, F.; Soulié, F. Microstructure and residual stresses in Ti-6Al-4V alloy pulsed and unpulsed TIG welds. *J. Mater. Process. Technol.* **2016**, *231*, 441–448. [CrossRef]

30. Rae, W.; Lomas, Z.; Jackson, M.; Rahimi, S. Measurements of residual stress and microstructural evolution in electron beam welded Ti-6Al-4V using multiple techniques. *Mater. Charact.* **2017**, *132*, 10–19. [CrossRef]

31. Mishurova, T.; Artzt, K.; Haubrich, J.; Requena, G.; Bruno, G. New aspects about the search for the most relevant parameters optimizing SLM materials. *Addit. Manuf.* **2019**, *25*, 325–334. [CrossRef]

32. Serrano-Munoz, I.; Mishurova, T.; Thiede, T.; Sprengel, M.; Kromm, A.; Nadammal, N.; Nolze, G.; Saliwan-Neumann, R.; Evans, A.; Bruno, G. The residual stress in as-built Laser Powder Bed Fusion IN718 alloy as a consequence of the scanning strategy induced microstructure. *Sci. Rep.* **2020**. under revision.

33. Martina, F.; Roy, M.; Colegrove, P.; Williams, S.W. Residual stress reduction in high pressure interpass rolled wire+arc additive manufacturing Ti-6Al-4V components. In Proceedings of the 25th International Solid Freeform Fabrication Symposium, Austin, TX, USA, 4–6 August 2014.

34. Boin, M.; Wimpory, R.C. E3: Residual Stress Neutron Diffractometer at BER II. *J. Large Scale Res. Facil. JLSRF* **2016**, *2*, 100. [CrossRef]

35. Mishurova, T.; Serrano-Munoz, I.; Thiede, T.; Ulbricht, A.; Sprengel, M.; Evans, A.; Kromm, M.; Madia, M.; Bruno, G. A critical discussion on the diffraction-based experimental determination of Residual Stress in AM parts. *Astm. Sel. Tech. Pap. (Stp)* **2020**, in press.

36. Thiede, T.; Cabeza, S.; Mishurova, T.; Nadammal, N.; Kromm, A.; Bode, J.; Haberland, C.; Bruno, G. Residual Stress in Selective Laser Melted Inconel 718: Influence of the Removal from Base Plate and Deposition Hatch Length. *Mater. Perform. Charact.* **2018**, *4*, 717–735. [CrossRef]

37. Szost, B.A.; Terzi, S.; Martina, F.; Boisselier, D.; Prytuliak, A.; Pirling, T.; Hofmann, M.; Jarvis, D.J. A comparative study of additive manufacturing techniques: Residual stress and microstructural analysis of CLAD and WAAM printed Ti–6Al–4V components. *Mater. Des.* **2016**, *89*, 559–567. [CrossRef]

38. Kröner, E. Berechnung der elastischen Konstanten des Vielkristalls aus den Konstanten des Einkristalls. *Z. Phys.* **1958**, *151*, 504–518. [CrossRef]

39. Burgers, W.G. On the process of transition of the cubic-body-centered modification into the hexagonal-close-packed modification of zirconium. *Physica* **1934**, *1*, 561–586. [CrossRef]

40. Kraus, W.; Nolze, G. POWDER CELL—A program for the representation and manipulation of crystal structures and calculation of the resulting X-ray powder patterns. *J. Appl. Crystallogr.* **1996**, *29*, 301–303. [CrossRef]

41. Rodrigues, T.A.; Duarte, V.; Miranda, R.M.; Santos, T.G.; Oliveira, J.P. Current Status and Perspectives on Wire and Arc Additive Manufacturing (WAAM). *Materials* **2019**, *12*, 1121. [CrossRef]

42. Ding, J.; Colegrove, P.; Mehnen, J.; Ganguly, S.; Almeida, P.S.; Wang, F.; Williams, S. Thermo-mechanical analysis of Wire and Arc Additive Layer Manufacturing process on large multi-layer parts. *Comput. Mater. Sci.* **2011**, *50*, 3315–3322. [CrossRef]

43. Hönnige, J.R.; Colegrove, P.A.; Ahmad, B.; Fitzpatrick, M.E.; Ganguly, S.; Lee, T.L.; Williams, S.W. Residual stress and texture control in Ti-6Al-4V wire + arc additively manufactured intersections by stress relief and rolling. *Mater. Des.* **2018**, *150*, 193–205. [CrossRef]

44. Martina, F.; Roy, M.J.; Szost, B.A.; Terzi, S.; Colegrove, P.A.; Williams, S.W.; Withers, P.J.; Meyer, J.; Hofmann, M. Residual stress of as-deposited and rolled wire+arc additive manufacturing Ti–6Al–4V components. *Mater. Sci. Technol.* **2016**, *32*, 1439–1448. [CrossRef]

45. Vila, M.; Prieto, C.; Zahr, J.; Pérez-Castellanos, J.L.; Bruno, G.; Jiménez-Ruiz, M.; Miranzo, P.; Osendi, M.I. Residual stresses in ceramic-to-metal joints: Diffraction measurements and finite element method analysis. *Philos. Mag.* **2007**, *87*, 5551–5563. [CrossRef]